Confinement of electron plasma by levitating dipole magnet

H. Saitoh, Z. Yoshida, J. Morikawa, Y. Yano, H. Hayashi, T. Mizushima, Y. Kawai, M. Kobayashi, and H. Mikami
Department of Advanced Energy, Graduate School of Frontier Sciences, University of Tokyo, 5-1-5 Kashiwanoha, Kashiwa, Chiba 277-8561, Japan

(Received 19 July 2010; accepted 20 October 2010; published online 15 November 2010)

A recent experiment on the Ring Trap 1 device has demonstrated long-term (exceeding 300 s) confinement of non-neutral (pure electron) plasma in a dipole magnetic field; particles diffuse inward, steepening the density gradient and self-organizing into a stable vortex structure [Z. Yoshida *et al.*, Phys. Rev. Lett. **104**, 235004 (2010)]. In this study, the internal structures of the plasma are experimentally investigated, and it is shown that the observations are consistent with rigidly rotating charged particle clump. The radial profiles of electrostatic potential and electron density consistently show that the drift velocity has homogeneous angular frequency in the confinement region. The electrostatic fluctuations also rotate rigidly with a phase velocity that agrees with the drift velocity. The magnetospheric system should have a wide application in confining single-species and even multiple-species charged particles. © *2010 American Institute of Physics*. [doi:10.1063/1.3514207]

I. INTRODUCTION

In a uniform straight magnetic field, axisymmetric non-neutral plasma of constant density rotates rigidly, creating a balance between the self-electric field and the induction ($\mathbf{v}\times\mathbf{B}$) electric field. On a rigidly rotating frame, the effective potentials cancel, and thus, the constant density is consistent with the Boltzmann (thermal) distributions.[1,2] In Malmberg and multiring traps where non-neutral plasmas are stably trapped by axial magnetic field and plugging electrostatic field, various studies on single-component non-neutral plasmas have been conducted.[3] Among other topics, the formation and confinement of antimatter plasmas are challenging issues in non-neutral plasma studies.[4] Antimatter plasmas are an interesting subject of study in its own right, but they also have a variety of scientific and technological applications. Simultaneous confinement of electron and positron plasmas enables experiments on pair plasmas,[5–8] and, in the future, it can potentially be used for laboratory studies of electron-positron plasma in space phenomena.[9] Stable confinement of low temperature electron and positron plasmas will enable production of a large number of positronium, which can be used for precision tests of the CP and CPT symmetries[10] and as a new γ-ray source.[11] An efficient trap system for non-neutral plasmas can also be used for storage of antimatter particles.[4] In studies of antimatter plasmas so far, interaction between positron plasma and electron beams[12,13] and formation of cold antihydrogen atoms for the stringent tests of the CPT symmetry[14–16] have been performed using the linear trap configurations. Confinement of toroidal plasmas with arbitrary nonneutrality[17,18] is the next major progress toward the experimental studies of electron-positron and antihydrogen plasmas.

Toroidal closed magnetic surface configurations are suitable for confining high-energy (or high-temperature) charged particles (Fig. 1). This configuration can also confine multiple-component plasmas, even with opposite-sign charges. We have started studies on toroidal non-neutral plasma in a dipole magnetic field.[17] Proto-RT[19–21] was a prototype magnetospheric device with a dipole field coil that was mechanically supported in the chamber. One of the key issues in the formation of toroidal non-neutral plasmas is the method of particle injection across the closed magnetic surfaces. In Proto-RT, effective electron injection into the closed surfaces was achieved using the effects of chaotic orbits of electrons due to magnetic null line and applied rf fields.[19] Current returned to the electron source decreased to less than 1%, and efficient electron injection was realized. Electron plasma with several kilovolts of space potential was steadily generated by continuous beam injection. In investigating the internal potential structures of electron plasma in Proto-RT,[20,21] we found that the confinement properties were drastically improved when the shapes of potential contours were adjusted to those of the magnetic surfaces by negatively biasing the case of the dipole field coil. The stable confinement time rose to more than 0.2 s, which is close to the classical diffusive loss time caused by the collisions with neutral molecules.

The reader is referred to several studies on toroidal non-neutral plasmas with different geometries.[22–27] Initial experiments on the toroidal non-neutral plasma were conducted in a pure toroidal field for the production of highly charged heavy ions trapped in a large negative potential well of electron plasma.[22] Similar to the case for neutral plasmas, charged particles are rapidly lost from the trap because of the drift motions in a pure toroidal field. Because of the strong self-electric field, however, forces due to induced image charges on the chamber wall can act as an effective rotational transform for non-neutral plasmas.[23] Recent experiments in a pure toroidal field have demonstrated feedback-controlled stabilization of the $m=1$ dioctoron mode and improved confinement times of up to 3 s.[24] Besides the magnetospheric traps, one can produce closed magnetic surfaces by external coil currents of the stellarator configurations, although the system is no longer axisymmetric. Experiments on pure electron plasma have been conducted in a helical system[26] and a

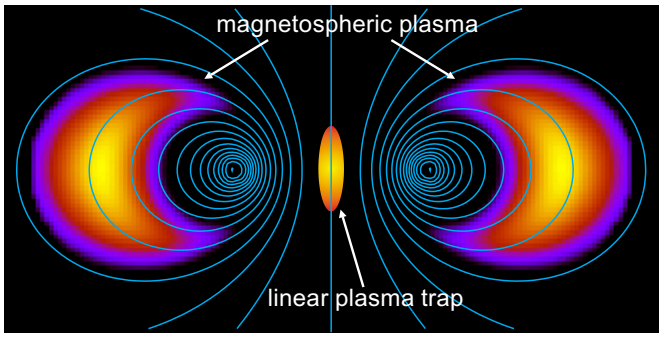

FIG. 1. (Color online) Dipole field lines generated by the ring current and plasma confinement regions. Magnetospheric plasma is confined by the dipole field and magnetic mirror effects, as shown by the image contours. Trapping non-neutral plasma in a linear trap is similar to trapping plasma in small region on the center axis of ring current.

stellarator with interlocking coils,[27] with the goal of conducting future experiments on confining electron-positron plasma.

Now, we return to the dipole confinement and describe recent developments. The Ring Trap 1 (RT-1) device is a successor to the Proto-RT experiment. It has a levitated superconducting magnet made with Bi-2223 high-temperature superconducting wires.[28,29] Although the coil levitation prevents disturbance to the confinement region, electrode biasing on the dipole field coil is impossible in RT-1, and we cannot artificially optimize the internal electrostatic potential profiles that are suitable for stable plasma confinement. We conducted a pure electron plasma experiment in RT-1 and realized a maximum confinement time of exceeding 300 s.[30] Although the potential profiles were not externally controlled, a stable confinement configuration was spontaneously generated. Here, a question arises as to what kind of internal structures can be stably and spontaneously sustained in the magnetospheric electron plasma. In this study, we experimentally studied the spatial structures and fluctuation properties of electron plasma in RT-1 by measuring the electrostatic potential and density profiles of plasma in a quasistable state during electron injection. We found that the toroidal $\mathbf{E}\times\mathbf{B}$ flow of plasma has a radially constant angular frequency, although the plasma is confined in a strongly inhomogeneous dipole field. We also observed that the plasma fluctuation has a radially coherent mode structure. These observations strongly suggest the spontaneous charging up of the levitated dipole field coil and the formation of a rigid-rotor stable equilibrium state of non-neutral plasma in the magnetospheric configuration. In the following sections, we describe these topics: Sec. II, the RT-1 experimental setup and measurement methods using a Langmuir probe and a wall probe; Sec. III, plasma formation and electron loss mechanism; Sec. IV, spatial structures of plasma and evidence of inward diffusion; Sec. V, fluctuation properties; and Sec. VI, observation of long confinement.

II. EXPERIMENTAL SETUP AND DIAGNOSTICS

Figure 2 shows a cross section of the RT-1 device and the structure of the electron gun. Inside the vacuum chamber,

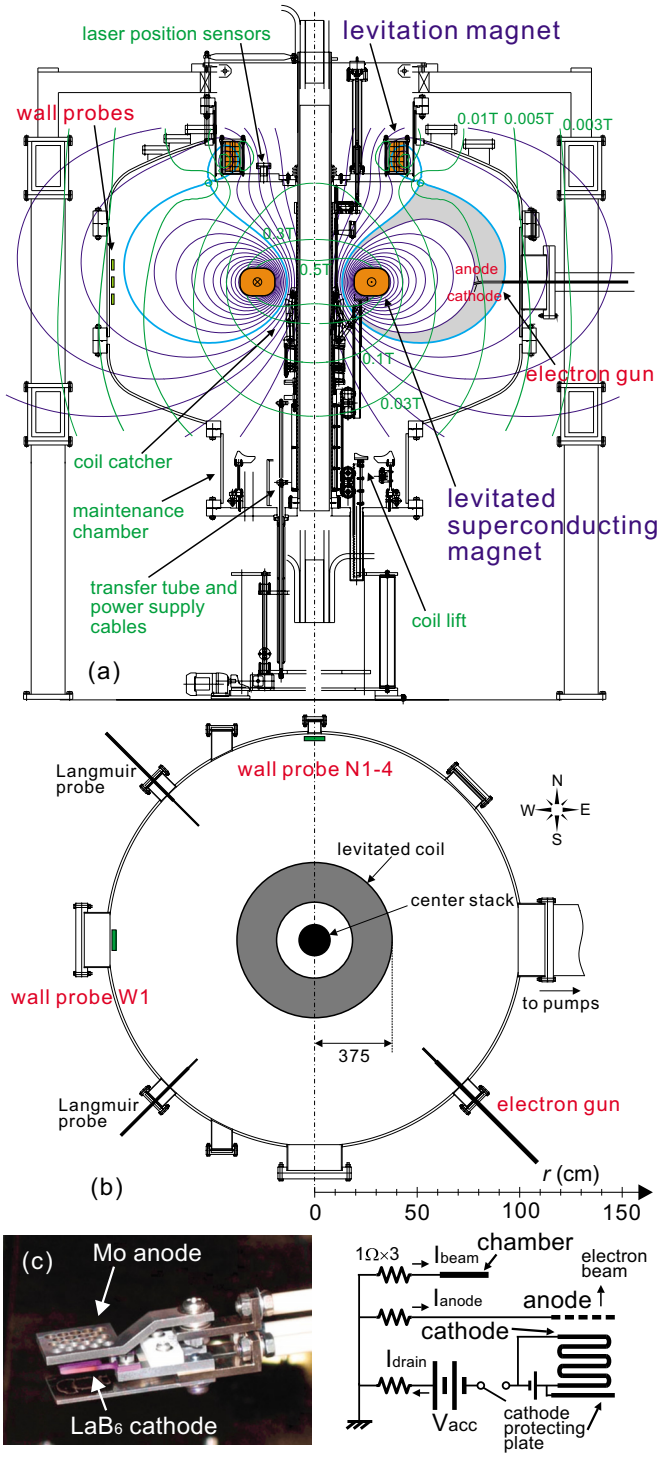

FIG. 2. (Color online) Experimental setup: (a) poloidal cross section and (b) top view of the RT-1 device including coil magnets, vacuum chamber, and electron gun. The thin lines show magnetic surfaces generated by a combination of levitated superconducting magnet and normal-conducting levitation magnet. (c) Photograph and circuit diagram of the electron gun.

RT-1 has a Bi-2223 high-temperature superconducting dipole field coil. The coil is magnetically levitated by a levitation coil located at the top of the chamber. The rated current values of the levitated and levitation coils are 250 and 28.8 kA, respectively. The magnetic separatrix is located at $r=92$ cm on the equatorial plane ($z=0$ cm) of the device. The vertical position of the superconducting coil is moni-

tored by three-cord laser sensors, and the current of the levitation coil is feedback-controlled to enable stable levitation. The vacuum chamber is 2 m in diameter and the base pressure is 7×10^{-7} Pa. More detailed explanations of the RT-1 device are found in Ref. 29.

As illustrated in Fig. 2(c), the electron gun consists of a LaB_6 cathode and a molybdenum anode located 2 mm apart from the cathode[19] and is located at the southeast port of RT-1. The cathode is heated by a dc of 24 A, and negatively biased to $-V_{acc}$ against the chamber wall for electron injection. The anode is electrically connected to the chamber, and electrons are injected with an initial energy of eV_{acc}. The gun is radially movable at the edge of the confinement region on the $z=0$ cm plane and can be rotated about the supporting rod. Drain, anode, and beam currents of the electron gun are monitored by 1 Ω resistors. To ensure that the external electron supply is stopped in the stable confinement phase, we switched off both V_{acc} and the cathode heating current after electron injection.

As a perturbation-free diagnostic tool for electrostatic fluctuations, we used wall probes[22] in RT-1. The wall tip is a stainless-steel foil located outside the confinement region in the chamber, and electrically connected to the chamber via a 100 kHz bandwidth current amplifier. The wall probes were used for measurements of radial electric field strength as well as frequency and amplitude of fluctuations in the edge region. The image current signal $I_i=dQ_i/dt$ is sent to an analog integration circuit to measure the average electric field strength on the wall

$$E_r=-\int dtI_i/\varepsilon_0 S, \tag{1}$$

where ε_0 is the vacuum permittivity and S is the wall area facing the plasma. The longest applicable integration time in the present experimental setup is about 10 s. More detailed description on the measurements of E_r and techniques for estimating the spatial profiles of plasma using wall probes are reported in Ref. 31.

For measurements of space potential ϕ_s in plasma, we installed an emissive Langmuir probe[20,21,26,32,33] on the northwest port of RT-1. The emissive probe was also used for the measurements of local electron density as a conventional Langmuir probe. The probe tip is a thoria-tungsten spiral filament of 0.1 mm diameter and 20 mm total length, and heated by a dc of 1.5 A. The tip was connected to a floating power source via tungsten wires that are covered by insulating alumina tubes. The probe was placed at $z=0$ cm and could be radially moved from $r=50$ to 100 cm in the confinement region. The insertion of the probe structure into the confinement region causes perturbation to the plasma and long time confinement is not realized. Therefore, we can use the Langmuir probes only during electron injection phase.

The local space potential can be identified as the point where the current-voltage (I-V) curves for an emissive probe with and without filament heating begin to deviate.[33] Using the emissive Langmuir probe, ϕ_s is also estimated by the so-called floating potential method. For the estimation of ϕ_s by the floating potential method in RT-1, the probe was electrically connected to the chamber via a 100 MΩ high-impedance voltage probe, and high-impedance potential ϕ_h was measured. Unlike the cases for neutral plasmas, floating potential ϕ_f is not defined for pure electron plasma. Assuming that electrons have Maxwellian distributions and neglecting the space charge effects, ϕ_h of an emissive Langmuir probe is written as

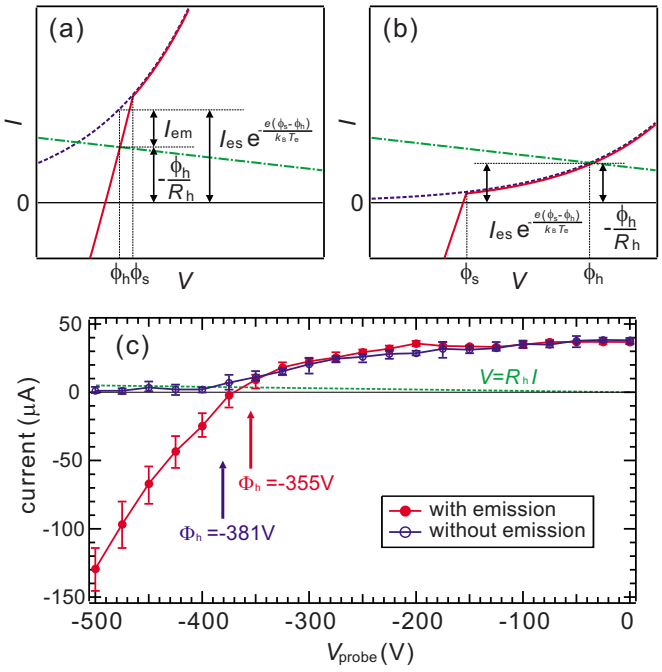

FIG. 3. (Color online) I-V characteristics of emissive (solid lines) and nonemissive (dotted lines) probes when (a) electron density is sufficiently high and (b) too low, respectively. The chain line shows the $V=-R_hI$ curve. (c) Typical I-V characteristics of hot (filled circles) and cold (nonemitting) (open circles) emissive Langmuir probe in RT-1. The space potential is estimated to be $\phi_s=-351$ V, where the two I-V curves begin to separate. The dotted line shows a working line of 100 MΩ high impedance. Measured high-impedance potentials are also plotted.

$$\phi_h=\phi_s-\frac{k_BT_e}{e}\ln\left(\frac{I_{es}}{I_{em}-\phi_h/R_h}\right), \tag{2}$$

where I_{es} is the electron saturation current, I_{em} is the emission current of thermal electrons, k_BT_e is the electron temperature, and R_h is the high-impedance value.[33] Figures 3(a) and 3(b) show the relation between ϕ_s and ϕ_h. When the electron current and emission current are sufficiently large, as shown in Fig. 3(a), ϕ_h of an emissive Langmuir probe gives good approximation of ϕ_s, satisfying $I_{es}\sim I_{em}-\phi_h/R_h$. When the electron density is low and sufficient electron current is not obtained, however, ϕ_s estimated by the floating potential method contains considerable errors [Fig. 3(b)].

We compared ϕ_h and the I-V characteristics of emissive probes with and without current heating (hot and cold probes) and found that in most cases, ϕ_s is close to ϕ_h measured by the emissive probe especially in weak field regions. Figure 3(c) shows typical I-V curves of the emissive Langmuir probe in RT-1 with and without filament heating. From the separation point of the two curves, we see that $\phi_s=-351$ V. As plotted in Fig. 3(c), ϕ_h is given at the intersection of the I-V curves and the $V=IR_h$ line. For the emis-

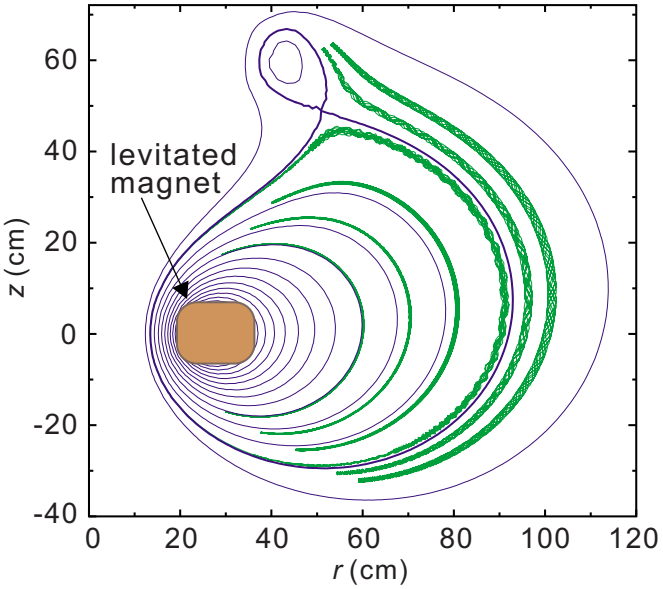

FIG. 4. (Color online) Calculated electron orbits and magnetic surfaces in RT-1. Each line is a single-particle trajectory in magnetic configuration of RT-1. Electrons are injected from $r=60$, 70, 80, 90, 95, and 100 cm at $z=0$ cm. Initial acceleration voltage $V_{acc}=500$ V.

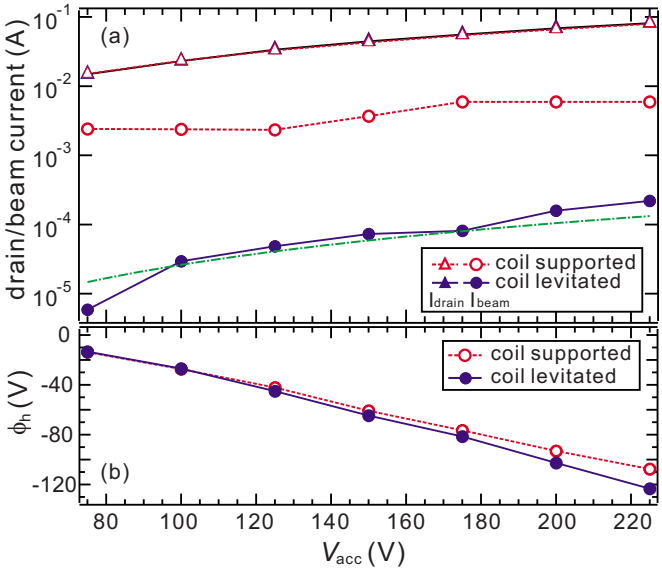

FIG. 5. (Color online) Dependencies on electron gun acceleration voltage with and without coil levitation (a) of drain current from cathode (triangles) and injected beam current (circles) from the electron gun and (b) of potential ϕ_h measured by edge Langmuir probe using high impedance at $r=80$ cm. The gun was located at $r_{gun}=80$ cm. The chain line shows I_{gun}, current absorbed by the electron gun structure located in the edge confinement region.

sive probe, $\phi_h=-355$ V is quite close to ϕ_s. While for the nonemissive probe, $\phi_h=-381$ V, which underestimates ϕ_s. We found that the difference between ϕ_s and ϕ_h becomes considerable especially in strong field regions. In such cases, we also measured the *I-V* curves to decide ϕ_s with and without heating current and kept the error less than 5%.

For an approximate estimate of ϕ_s in the edge trap region ($r=80-100$ cm), and especially for measurements of radial electric field strength E_r, a nonemissive Langmuir probe was also installed at a north port of the chamber. We see from Eq. (2) that a nonemissive probe satisfies $\phi_h=\phi_s-\alpha k_B T_e/e$, where α is a constant decided by the ratio of electron saturation current and ϕ_h.[33] We can estimate E_r reliably from two ϕ_h measured at different positions with a cold probe, as far as the distance Δx of two measuring points is short enough and the spatial variations of α and T_e are small, resulting in $\Delta\phi_h \sim \Delta\phi_s$. We found that E_r measured by a cold probe agrees well with that measured by an emissive probe typically within an error of 10% in the edge confinement region when $\Delta x=1$ cm.

A rake probe with 10 channel stainless-steel tips was also used in RT-1 for simultaneous measurements of electrostatic fluctuations. The rake probe was covered with a ceramic tube with 25 mm diameter, and the probe tips were spaced 2 cm apart along the radial direction.

III. PLASMA FORMATION BY BEAM INJECTION AND ELECTRON LOSS MECHANISM

Figure 4 shows the calculated orbits of an electron projected on the poloidal cross section in the magnetic field configuration of RT-1 generated by the levitated and levitation magnets. In a toroidal symmetric geometry, the canonical angular momentum P_θ of a trapped charged particle is temporally constant.[2] The spatial deviation of a particle from the initial magnetic surface is then less than the poloidal Larmor radius: $d \leq |mr\dot{\theta}/eB_p| = r_p$, where m_e is the electron mass, e is the charge, and $B_p=(B_r^2+B_z^2)^{1/2}$ is the poloidal magnetic field strength. In RT-1, the electron Larmor radius is at most 7.5 mm in the edge confinement region for $T_e=500$ eV, and the motion of a single charged particle is localized near the initial vacuum magnetic surfaces as shown in the figure. Estimation of T_e during stable confinement phase is not straightforward and was not investigated in the present study.

In RT-1, we inject electrons into the static magnetic field from an electron gun located in the edge confinement region. As plasma is generated inside the separatrix and reaches a steady state during gun operation, the electrostatic potential of the plasma becomes approximately constant. In this phase, the injected beam current is balanced by the sum of the loss currents. Loss channels for electrons include the mechanical structure of the gun located inside the separatrix and radial diffusions caused by neutral collisions and fluctuations. Without coil levitation, another major loss channel is the support structure of the superconducting coil.

We separated these loss channels by comparing the beam currents and plasma potentials by changing experimental conditions. First, we checked the effects of coil levitation. Figure 5 shows the dependencies of three variables on V_{acc}: drain current I_{drain} from the cathode, electron beam current I_{beam}, and high-impedance potential ϕ_h at $r=80$ cm measured by the edge Langmuir probe. Electrons were injected from $r=80$ cm in the upward direction as V_{acc} was varied from 75 to 225 V. Open circles and triangles in the figure show data for the supported dipole field coil, and filled circles and triangles show data for the levitated coil. When not levitated, the dipole field coil was operated at 90% of its

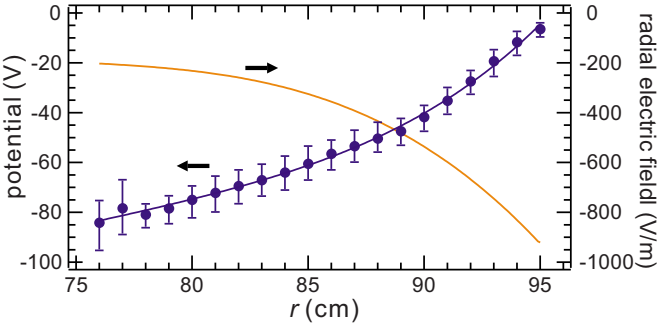

FIG. 6. (Color online) Radial profiles of high-impedance potential and radial electric field strength in the edge plasma region: $V_{acc}=175$ V and $r_{gun}=80$ cm.

rated current. The shapes of the magnetic surfaces in both cases were quite similar, and thus, the variation in plasma properties is attributed solely to the effects of the coil support structure. As shown in Fig. 5(a), coil levitation drastically reduced I_{beam}, and reduced the electron loss current to the order of 1%. Meanwhile, variations in ϕ_h were relatively small, implying that the number of trapped electrons was not substantially changed by coil levitation, as shown in Fig. 5(b). Since the plasma was approximately steadily sustained during electron gun operation, we can estimate the confinement time of electrons as $\tau=Q/I_{beam}$, where Q is the total charge of the plasma. The reduction of I_{beam} by coil levitation therefore indicates suppression of electron loss and increased confinement times caused by the removal of the coil support structures. The typical confinement time of electrons during beam injection is $\tau_l=100$ μs with coil levitation and $\tau_s=10$ μs without coil levitation.

According to wall probe measurements,[31] electrons on the magnetic surfaces intersecting the electron gun structure are selectively lost just after the electron supply ends. This indicates that the main loss channel for electrons, when the coil is levitated, is the gun structure located in the edge confinement region. Loss current due to collisions of electrons with the gun structure may be written as

$$I_{gun}=en_e v_{\mathbf{E}\times\mathbf{B}}S\propto V_{acc}^2, \tag{3}$$

where $S=0.64$ m^2 is the area of the magnetic surfaces projected onto the poloidal cross section that intersects the gun structure [hatched region in Fig. 2(a)], $v_{\mathbf{E}\times\mathbf{B}}=E_r/B$ is the toroidal $\mathbf{E}\times\mathbf{B}$ drift velocity, and $B=0.03$ T is the typical magnetic field strength in this region. Because ϕ_h is an approximately a linear function of V_{acc} [Fig. 5(b)], indicating that the plasma potential is decided primarily by the injected electron energy, and the shapes of the ϕ_h profiles are similar for various V_{acc}, we assumed that n_e and E_r are proportional to V_{acc}. Figure 6 shows radial profiles of ϕ_h and calculated E_r in the edge confinement region. With $V_{acc}=175$ V, the typical value of E_r is 300 V/m in the edge region. The observed potential profile is well reconstructed by an electron number density of $n_e=5\times10^{10}$ m^{-3} in the edge confinement region. A chain line in Fig. 5(a) shows a plot of I_{gun} calculated using these values and assumptions. I_{gun} approximately balances I_{beam}, indicating that the electron loss during beam injection is caused primarily by the electron gun structure located inside the separatrix. We note that electron loss due to the gun structure arises only in the edge confinement region, and therefore, we did not evaluate here the confinement properties of the long-lived component of electrons trapped in the strong field region.

Another loss mechanism for electrons is collision with the remaining neutral molecules. From the fluid equation for electrons with finite temperature T_e, including the effects of collisions with neutrals, in addition to single-particle motion in static electric and magnetic fields,

$$m_e n_e\frac{d\mathbf{v}}{dt}=-e(\mathbf{E}+\mathbf{v}\times\mathbf{B})-k_B T_e\nabla n_e-m_e n_e\nu_{ne}\mathbf{v}, \tag{4}$$

the perpendicular velocity of the electrons is given by

$$\mathbf{v}_\perp=-\frac{k_B T_e\nabla n_e/n_e+e\mathbf{E}}{m_e\nu_{ne}[1+(\omega_c/\nu_{ne})^2]}+\frac{\mathbf{v}_{\mathbf{E}\times\mathbf{B}}+\mathbf{v}_D}{1+(\nu_{ne}/\omega_c)^2}, \tag{5}$$

where $\mathbf{v}_{\mathbf{E}\times\mathbf{B}}=\mathbf{E}\times\mathbf{B}/B^2$ and $\mathbf{v}_D=\nabla(n_e k_B T_e)\times\mathbf{B}/en_e B^2$ are the $\mathbf{E}\times\mathbf{B}$ and diamagnetic drift velocities. Because the electrons are magnetized and the condition $\omega_c\gg\nu_{ne}$ is satisfied, the vertical motion of electrons across the magnetic surfaces is approximated as

$$\mathbf{v}_{n\perp}\sim-\frac{k_B T_e\nu_{ne}}{m_e\omega_c^2}\frac{\nabla n_e}{n_e}-\frac{e\nu_{ne}}{m_e\omega_c^2}\mathbf{E}=-D_{n\perp}\frac{\nabla n_e}{n_e}-\mu_\perp\mathbf{E}, \tag{6}$$

where ν_{ne} is the electron-neutral collision frequency, $D_{n\perp}$ is the diffusion coefficient, and $\mu_\perp$ is the mobility term in the perpendicular direction. Substituting the typical values of $B=0.03$ T, $T_e=100$ eV, $P_n=10^{-6}$ Pa, and $n_e=10^{12}$ m^{-3}, we have $D_{n\perp}=1\times10^{-4}$ m^2 s^{-1}, $\mu_\perp=1\times10^{-6}$ V^{-1} m^2 s^{-1}, and $v_{n\perp}$ is of the order of 10^{-3} ms^{-1}. The cross field current of electrons due to neutral collisions is then estimated to be

$$I_{n\perp}=en_e v_{n\perp}A\sim10^{-10}\ \text{A}, \tag{7}$$

where $A\sim1$ m^2 is the typical area of a magnetic surface. Because $I_\perp$ is more than four orders of magnitude smaller than I_{gun} in the present experimental conditions, the effects of neutral collisions on the injection and loss current balance are negligible in the electron injection phase. In fact, variations in neutral gas pressure in the low pressure range do not seriously affect plasma properties. This is evident in Fig. 7, which shows the effects of P_n on space potential, electron gun current, and dominant fluctuation frequency during electron injection. These parameters are independent of P_n below approximately 10^{-5} Pa where most of the experiments are conducted. The effects of neutral molecules become nonnegligible above approximately 10^{-4} Pa, and stable confinement is not realized in this pressure range, as described in the following sections. We note that at base pressure of 7×10^{-7} Pa, ion current was not observed by a Langmuir probe within the measurement error, indicating that the ratio of ions in plasma is at least less than 10%. This is possibly because ions generated by collisions of electrons and neutrals are lost and balanced due to volume and surface recombination processes.[34]

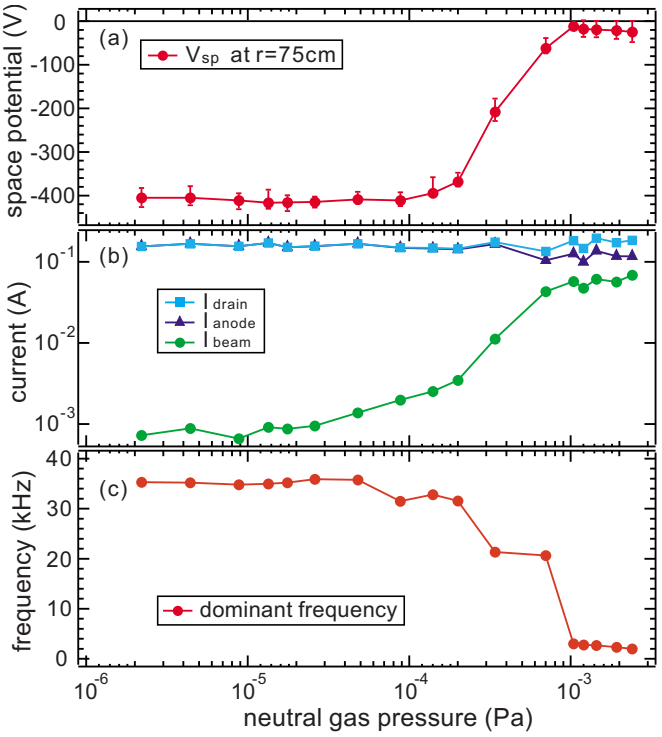

FIG. 7. (Color online) Dependencies on filled neutral (helium) gas pressure (a) of the high-impedance potential of the emissive Langmuir probe, (b) of the electron gun current, and (c) of the dominant electrostatic fluctuation frequency. The gun was located at $r_{gun}=80$ cm and $V_{acc}=500$ V.

IV. SPATIAL STRUCTURES AND INWARD DIFFUSION OF PLASMA

Figure 8 shows the radial space potential profiles during beam injection, measured by the emissive Langmuir probe with and without coil levitation. During operation without coil levitation, the dipole field coil was operated at 90% of its rated value to ensure that the shapes of the magnetic surfaces would be similar to their shapes during operation with coil levitation. Electrons were injected from $r_{gun}=80$ cm with $V_{acc}=500$ V. When the coil was not levitated (open circles and dotted line), the gradient of ϕ_s is close to 0 at $r \approx 65$ cm, where ϕ_s approaches minimum value. Because the stainless-steel case of the superconducting magnet is electrically connected to the chamber through the support structure without coil levitation, $\phi_s=0$ V on the coil case surface at $r=37.5$ cm. The potential profile is, therefore, always convex downward without coil levitation, and the toroidal $\mathbf{E}\times\mathbf{B}$ drift motion has a strong shear flow, which may lead to the destabilization of the plasma. Without coil levitation, the grounded coil case and support structure are serious loss routes of electrons. In this case, long time confinement is not realized.

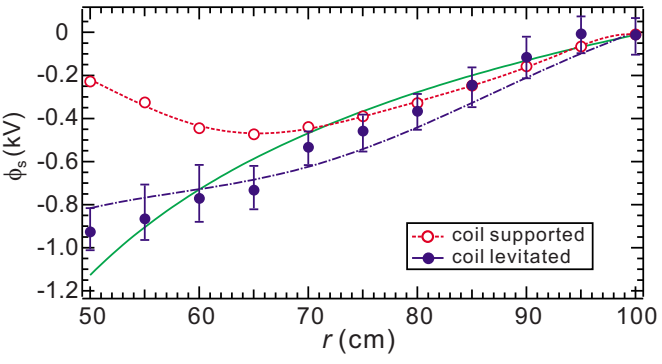

FIG. 8. (Color online) Radial profiles of space potential during beam injection with (filled circles) and without (open circles) coil levitation. The solid line shows the space potential profile that corresponds to rigid-rotor $\mathbf{E}\times\mathbf{B}$ rotation in the toroidal direction with $\omega=1.9\times10^5$ rad/s. The electron gun was located at $r_{gun}=80$ cm and operated with $V_{acc}=500$ V. The outer surface of superconducting coil is at $r=37.5$ cm and chamber wall is at $r=100$ cm. The chain line is the potential profile calculated from density profile in Fig. 11(b).

The filled circles in Fig. 8 show the ϕ_s profile with coil levitation. The potential profile has a relatively steep gradient because the superconducting coil is electrically floating and negatively charged against the chamber wall. Interestingly, ϕ_s in the stronger magnetic field region at $r<r_{gun}$ is substantially lower than $-V_{acc}$, indicating that electrons obtain extra energy and are radially transported inward from the initial position of the electron gun. Because of the small Larmor radius of the magnetized electron, the single-particle orbits of electrons are localized near the initial magnetic surface. The electrons may be radially transported because of the collisions with neutral molecules. However, the formation of a space potential below $-V_{acc}$ indicates that the total energy of the electrons at $r<r_{gun}$ is higher than the initial energy, which is not explained by diffusion caused by neutral collisions.

Cross field penetration and energization of charged particles are commonly observed in planetary magnetospheres.[35–37] Fluctuations in plasma with time scales faster than or comparable to the toroidal rotation period can violate the third adiabatic invariant $K=\int P_\theta ds \simeq e\Phi$, where $P_\theta=m_e r v_\theta+erA_\theta$ is the canonical angular momentum and Φ is the magnetic flux enclosed by the drift trajectory.[38] Then, the trajectories of the charged particles can deviate from the initial magnetic surface and the particles are radially transported. If the first invariant $\mu=m_e v_\perp^2/2B$ and the second invariant $J=\int m_e v_\parallel dl$ are conserved in this process, the perpendicular and parallel kinetic energies of the charged particles increase, as the particles are transported to stronger magnetic field regions. In RT-1, the plasma undergoes large electrostatic fluctuations in the diocotron frequency range during electron injection that can break the conservation of P_θ and K and causes radial penetration of the electrons. This can explain the experimental observation of the inward diffusion and energization of the electrons.

Figure 9 shows plots of electrostatic fluctuation and space potential as a function of V_{acc}. As V_{acc} is increased and the fluctuation amplitude grows, ϕ_h exceeds V_{acc} significantly, which is consistent with fluctuation-induced inward transport and energy enhancement of the electrons. Figure 10 shows further side evidence of fluctuation-induced radial transport. Electrons were injected by a gun located at $r=80$ cm. Particle flux was measured by a Langmuir probe located in the edge confinement region at $r=90$ cm. In the confinement phase after the electron injection from $t=0$ to 0.32 s, we observed simultaneous temporal activation of both electrostatic fluctuation and particle flux. These observations

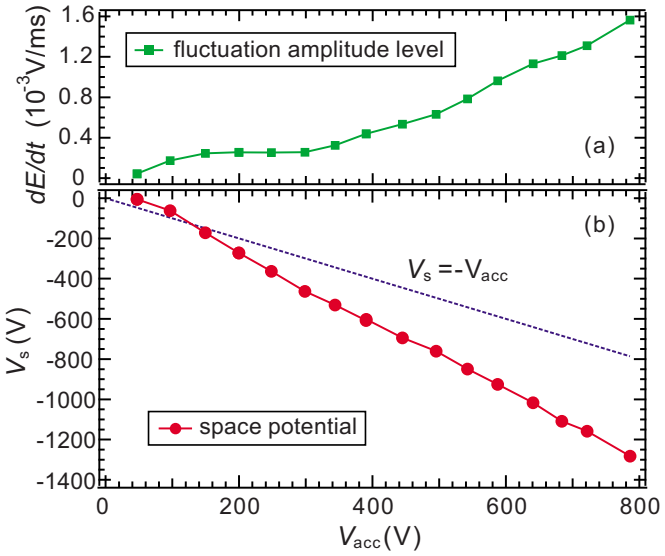

FIG. 9. (Color online) Dependencies on acceleration voltage of electron gun at $r=70$ cm (a) of electrostatic fluctuation measured by a wall probe and (b) of high-impedance potential measured by an emissive probe at $r=60$ cm.

are consistent with the transportation of electrons across the closed magnetic surfaces due to the activated fluctuations.

The solid line in Fig. 8 shows the space potential profile where the $\mathbf{E}\times\mathbf{B}$ drift velocity of the plasma is a rigid-rotor motion,

$$\phi_s = \omega \int Brdr, \tag{8}$$

where ω is the constant angular frequency of the toroidal rotation of the plasma. Here, we approximate that the plasma is horizontally symmetric near the $z=0$ cm plane and the z component of $\mathbf{E}$ can be neglected because the levitated coil current is much larger than the levitation coil current. As shown later in Fig. 13, the fluctuation frequency of the fundamental mode measured by the wall probe and the emissive probe is 31 kHz, and $\omega=1.9\times10^5$ rad/s. The $\mathbf{E}\times\mathbf{B}$ drift velocity of the plasma approximately agrees with the velocity of a toroidal rigid rotation with constant ω, as shown in

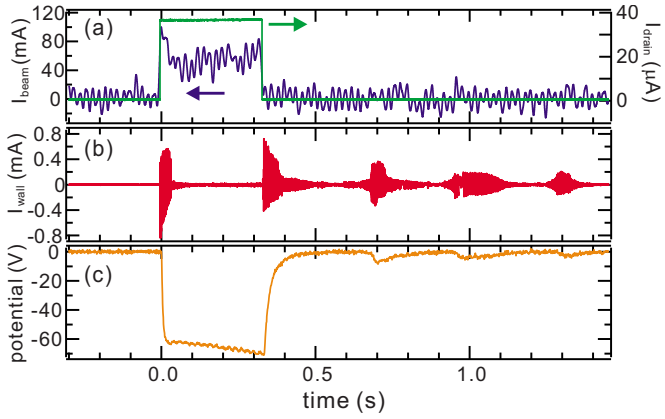

FIG. 10. (Color online) (a) Drain and beam currents of electron gun at $r_{gun}=80$ cm, (b) electrostatic fluctuation measured by wall probe, and (c) electrostatic particle flux measured by a Langmuir probe at $r=90$ cm.

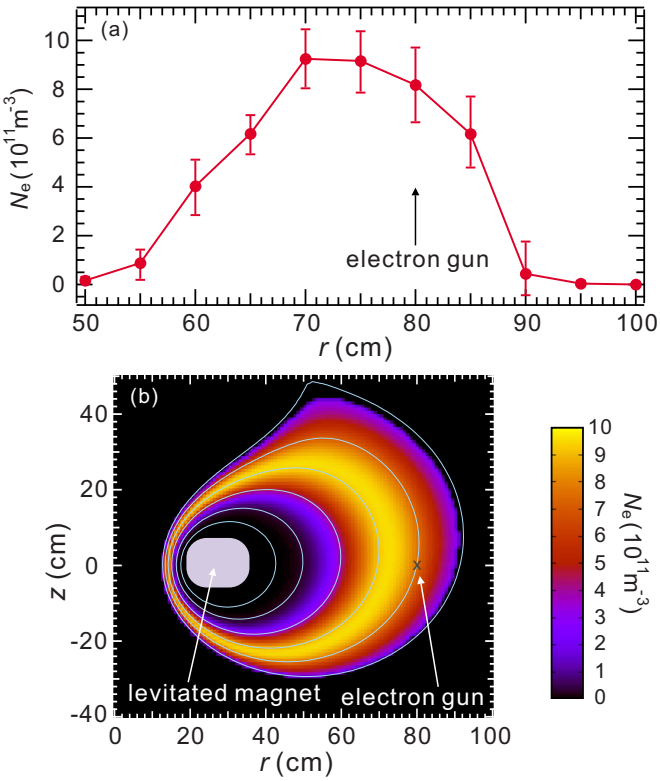

FIG. 11. (Color online) Plasma density profiles: (a) radial density profiles during beam injection, measured by electrostatic Langmuir probe located at $z=0$ cm. (b) Estimated density profile on the r-z plane, assuming that density is constant on magnetic surfaces.

Fig. 8. The ϕ_s curve does not entirely agree with the potential profile for rigid-rotor $\mathbf{E}\times\mathbf{B}$ motion, especially in the strong field region and near the electron gun, indicating the existence of some remaining differential motion in the rotation speed of the plasma during electron injection. As shown later in Fig. 12, the frequency power spectrum of the fluctuation has broad peaks in this phase. After the electron supply ends, the plasma undergoes long-lived stable fluctuation with a peaked frequency spectrum, which implies self-organization of a shear-free rigid-rotating stable equilibrium state. When the superconducting magnet is not levitated, the ϕ_s curve deviates greatly from the potential profile for rigid-rotor $\mathbf{E}\times\mathbf{B}$ motion.

Figure 11(a) shows the density profile of the plasma at $z=0$ cm, measured by the emissive probe used as a conventional Langmuir probe. The experimental conditions are the same as those for Fig. 9 ($r_{gun}=80$ cm and $V_{acc}=500$ V, and the superconducting magnet was levitated). The electrons are distributed inside the separatrix, transported inward across the magnetic surfaces from the position of the electron gun. Since the variation in f_{wall} as a function of r_{probe} is small (Fig. 13), it is reasonable to suppose that the density profile is not substantially distorted due to insertion of the emissive probe structure. Assuming that density n_e is constant on a magnetic surface [Fig. 11(b)], the space potential profile can be calculated, as shown in Fig. 8, as a chain line. Because the internal space potential results primarily from the majority of the electrons being trapped in weak field regions, the mirror effects of the trapped electrons are neglected in this approxi-

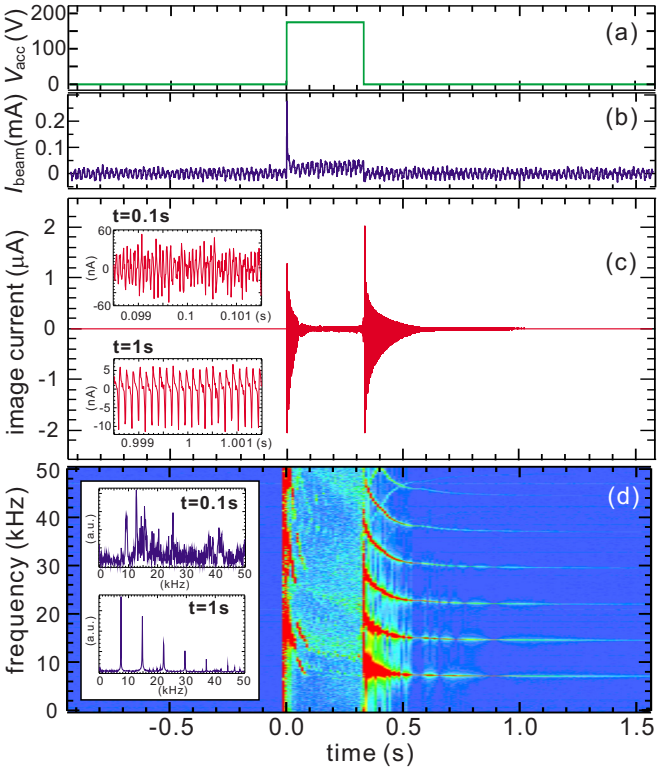

FIG. 12. (Color online) Formation and stabilization of electron plasma. (a) Electron gun acceleration voltage, (b) injected beam current, (c) electrostatic fluctuation, and (d) associated power spectra (Ref. 30).

mation. We did not measure the electrostatic potential V_{ic} of the levitated magnet case, but we estimated it to be -1210 V by extrapolating the ϕ_s curve. The chain line in Fig. 8 shows fairly good agreement with the measured ϕ_s profile, indicating that the n_e measurements are consistent with those of ϕ_s.

V. STABILIZATION AND FLUCTUATION PROPERTIES

Figure 12 shows V_{acc}, I_{beam}, electrostatic fluctuation, and the associated power spectrum in the injection and stabilization phases of the electron plasma. Electrons were injected with $V_{acc}=175$ V from $t=0$ to 0.32 s from the electron gun at $r=80$ cm. As electrostatic potential was built up in the initial injection phase, the injected electron beam was repelled and I_{beam} dropped from 300 to 10 μA before $t=50$ ms. The initial large turbulence decayed with a similar time constant, and, after this phase, the plasma was approximately in a steady state. As shown in Fig. 12(c), the fluctuating electric field has a complex spectrum with multiple frequencies during beam injection, especially in the initial turbulent phase. After beam injection ends, fluctuation increases again and then relaxes to a quiescent state. In this phase, the fluctuation spectrum has strongly peaked profiles.

Figure 13 shows the fundamental frequency of fluctuation measured by the wall probe f_{wall} and by the emissive probe f_{probe} as function of the radial probe position r_{probe}. The error bars for each data point indicate the full width at half maximum of the fundamental frequency peak. The variation in frequency due to probe insertion is less than 10%. The

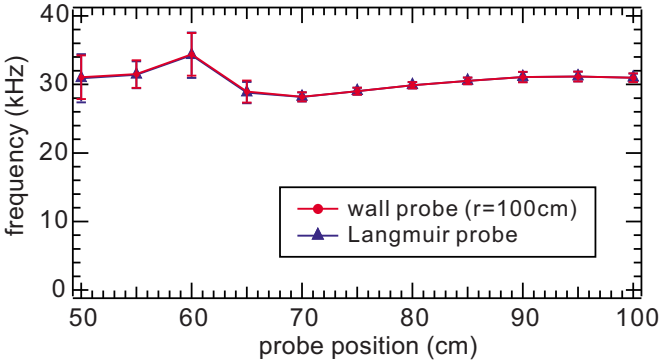

FIG. 13. (Color online) Fundamental frequency of fluctuation vs radial probe position measured by a wall probe located outside of the confinement region (circles) and by a Langmuir probe inserted into plasma (triangles).

effects of probe insertion are noticeable only at $r_{probe} \leq 60$ cm, where the frequency peaks of the fluctuation spectrum broaden, indicating increased disturbance due to the probe structure. In the same experimental shot, f_{probe} and f_{wall} agree within an error of 0.5%, indicating that the frequency of fluctuation is the same for different radial positions.

To measure the frequency and phase differences at different radial positions at the same toroidal and poloidal positions, we performed simultaneous measurements of electrostatic fluctuations with a 10 channel rake probe. Figure 14 shows the dominant frequencies observed by each probe tip and the associated waveforms, together with f_{wall}. The probe tips were electrically connected to the chamber via 10 kΩ resistors, and the fluctuation of the collected electron current was measured. The mechanical structure of the rake probe is

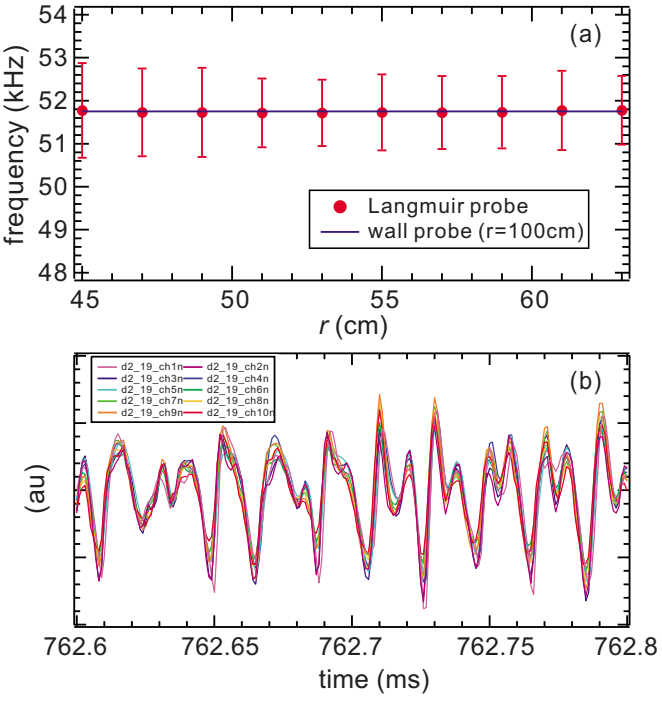

FIG. 14. (Color online) Electrostatic fluctuation at different radial positions. (a) Simultaneously measured frequencies and (b) associated waveforms. Vertical scales of the various signals are adjusted to simplify comparison of the phase differences.

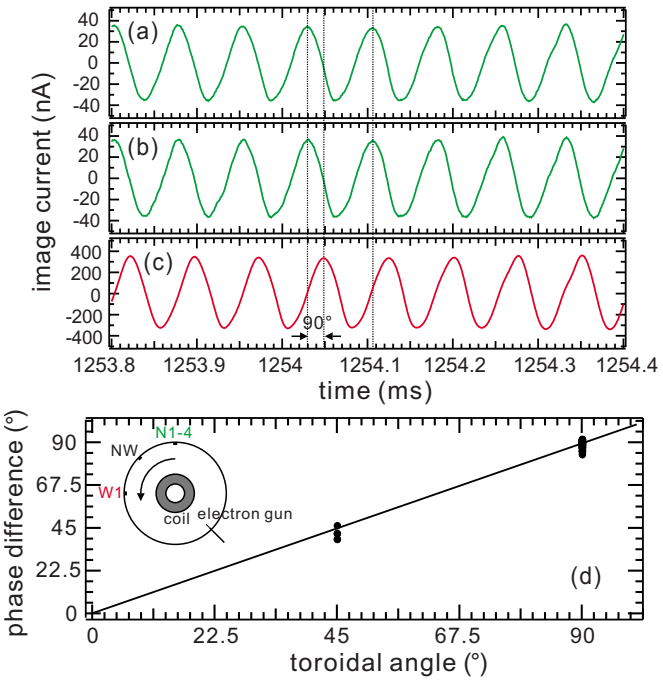

FIG. 15. (Color online) Electrostatic fluctuations at different toroidal and poloidal positions. Waveforms observed by wall probes (a) N2, (b) N4, and (c) W1, respectively. (d) Phase differences observed by wall probe pairs with toroidal separations of 45° (N2 and NW1) and 90° (N2 and W1). The inset shows a top view of RT-1, including the wall probes and the toroidal $\mathbf{E}\times\mathbf{B}$ drift direction of the negatively charged plasma.

larger than that of the emissive probe, resulting in relatively greater disturbance to the plasma. Possibly due to the disturbance, the predominant mode frequencies observed were $n=2$ rather than the fundamental mode, in contrast to the situation without rake probe insertion. Figure 14(a) shows the dominant $n=2$ mode frequencies. Figure 14(b) shows that the fluctuation waveforms are perturbed, presumably due to the insertion of the rake probe. The predominant fluctuation frequencies are constant at different radial positions and are the same as for f_{wall} observed outside the confinement region. The phase differences $\Delta\theta$ in the fluctuations observed at different radial positions are small, indicating that the plasma fluctuation is almost coherent in structure in the radial direction. We calculated the cross correlation of each of the rake probe signals and found that $\Delta\theta\leq 25°$ during electron injection.

We also measured fluctuation at different toroidal and poloidal positions and found that the oscillation mode propagates in the toroidal $\mathbf{E}\times\mathbf{B}$ drift direction. Figure 15 shows the waveforms of simultaneously measured fluctuations in the stable confinement phase. Walls N2 and N4 were located at the same poloidal cross section, and the toroidal separation between N2/N4 and W1 was 90°. As shown in Fig. 15(d), W1 was located at the downstream side of the $\mathbf{E}\times\mathbf{B}$ velocity of the negatively charged electron plasma. The signals from N2 and N4 are synchronous, and the fluctuation shows no phase difference in the poloidal direction [Figs. 15(a) and 15(b)]. The signal from W1 shows a phase delay of 90° from the signal from N2 and N4 [Fig. 15(c)]. Figure 11(d) shows a plot of the phase differences of wall probe signals for different toroidal separations. The separation angles agree with the phase differences, indicating that the toroidal mode number of the lowest observed frequency oscillation is $n=1$.

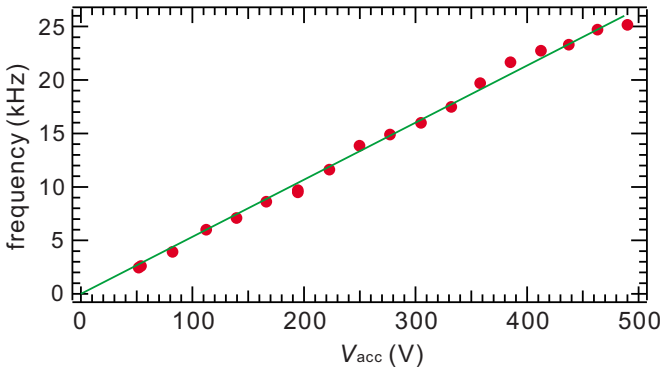

FIG. 16. (Color online) Frequencies of electrostatic fluctuation during electron injection vs electron gun acceleration voltage. The superconducting coil was mechanically supported in a pure dipole field (open circles) or was magnetically levitated (filled circles).

Figure 16 shows electrostatic fluctuation frequency as a function of V_{acc}. Frequency varies approximately linearly with V_{acc}. Because ϕ_{s} and E_{r} also vary approximately linearly with V_{acc}, it suggests that the frequency is proportional to E_{r}. The frequency of the dominant $n=1$ component of the mode is also close to the $\mathbf{E}\times\mathbf{B}$ rotation frequency. These observations are consistent with the frequency and propagation properties of the diocotron (Kelvin–Helmholtz) mode in a pure poloidal field configuration.

VI. STABILIZATION AND LONG TIME CONFINEMENT

Finally, we examined the long time confinement properties of electron plasma. Figure 17 shows the electrostatic fluctuation, associated power spectra, radial electrostatic field strength, and estimated spatial profiles of the plasma. Radial electric field strength and spatial profiles were measured and estimated using wall probes consists of stainless-steel foils, current amplifiers, and analog integration circuits.[31] In the steady state during electron injection, electrons fill approximately the entire region inside the separatrix. After the end of injection, electrons on the magnetic surfaces intersecting the electron gun structure are lost with a time constant of $\tau_{\mathrm{l}}=0.14$ ms, close to the toroidal rotation time of electrons with the $\mathbf{E}\times\mathbf{B}$ velocity, indicating that the electron gun structure creates a channel for electron loss in the edge confinement region, as described in Sec. III.

In the stable confinement phase, electrostatic fluctuation shows a peaked spectrum with a dominant frequency of 10 kHz and its higher harmonics. The spectrum slowly changes during confinement, indicating spatial variation of the plasma in the inhomogeneous field configuration. The stable phase lasts for more than 300 s and ends with rapid growth of instability. The observed confinement time is on the same order as the diffusion time caused by neutral collisions. As shown in Fig. 17(a), the instability typically grows with a time constant of 200 μs, and decays with a time constant of 30 ms. The electrons are lost at this point on a similar time scale [Fig. 17(c)(2)]. Figure 18 shows a plot of stable con-

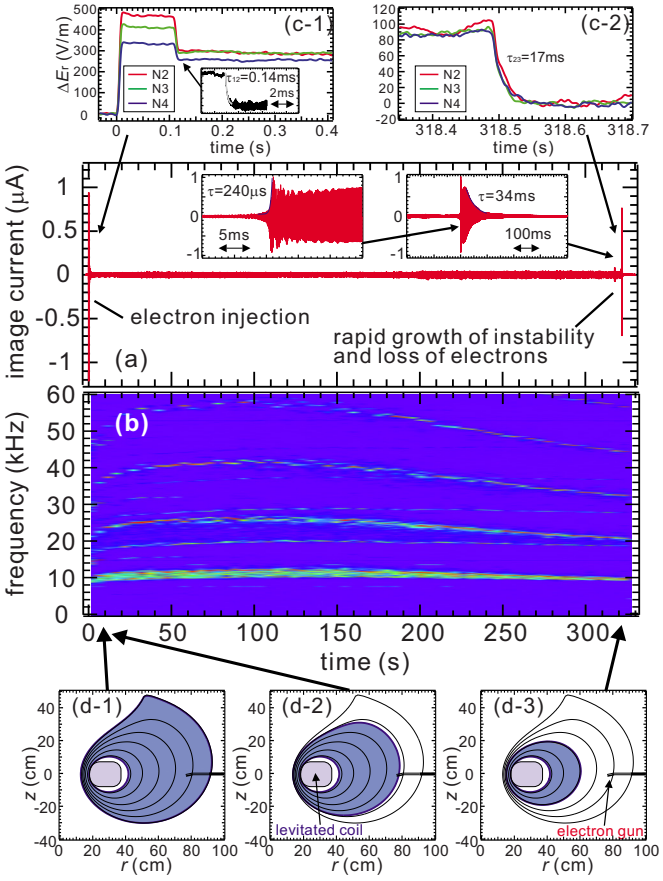

FIG. 17. (Color online) Long time confinement properties of electron plasma. (a) Electrostatic fluctuation, (b) associated power spectrum, and (c) radial electrostatic filed strength measured by a wall probe (1) when electrons are injected and (2) at the end of confinement. (d) Estimated spatial profiles of plasma (1) during electron injection, (2) just after the end of electron supply, and (3) at the end of confinement (Ref. 30).

finement time τ^* as a function of the filled neutral gas pressure P_n. Long confinement is realized below approximately 7×10^{-5} Pa. In the low pressure range, we found the empirical relationship $\tau^*\sim2.4\times P_n^{-0.35}$ s, which deviates from the linear relationship $\tau^* P_n$=const. The instability growth is possibly caused by ion resonance instability[39,40] due to ionization of residual neutral gas.

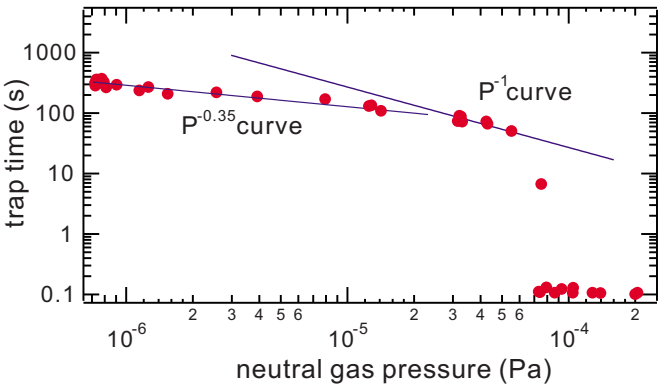

FIG. 18. (Color online) Stable confinement time of plasma in variation of neutral gas (hydrogen) pressure (Ref. 30).

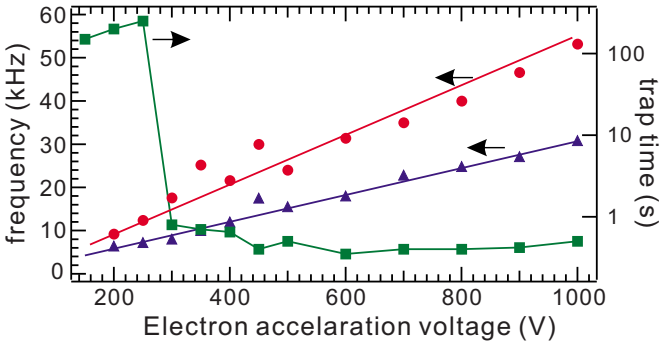

FIG. 19. (Color online) Dependencies on electron gun acceleration voltage of stable confinement time (squares), and fundamental fluctuation frequencies during electron beam injection (circles) and after electron injection ended (triangles).

Figure 19 shows the dependence of τ^* on V_{acc}. Stable confinement is realized when electrons are injected with $V_{acc}\leq250$ V. For $V_{acc}\geq300$ V, the plasma is not stabilized and long confinement is not realized after the electron supply ended. Possible reasons for the shortened confinement time with larger V_{acc} include instabilities caused by the steeper potential profiles due to a large number of initially trapped electrons and formation of ions.

VII. CONCLUSION

Stable confinement of non-neutral plasma has been realized in the magnetospheric configuration, and electrons with a density of the order of 10^{11} m^{-3} were trapped for more than 300 s. In this report, we presented experimental evidence for spontaneous formation of the stable confinement configuration of magnetospheric non-neutral plasma in RT-1. After electrons are injected from an electron gun located in the edge confinement region, they are transported inward to strong field region across the closed magnetic surfaces. We measured radial profiles of their electrostatic potential and electron density in a quasisteady state during beam injection and found that the toroidal $\mathbf{E}\times\mathbf{B}$ drift velocity of the plasma has approximately constant angular frequencies. During injection, the electrostatic fluctuation spectrum has broad peaks due to remaining small differential rotation. After the electron supply ends, the plasma settles into a long-lasting quiescent state with highly coherent fluctuations. These observations support the hypothesis of relaxation or self-stabilization of diocotron (Kelvin–Helmholtz) instabilities, which is a well-known process in the homogeneous magnetic field of a standard linear trap and indeed operates even in a strongly inhomogeneous dipole magnetic field.

ACKNOWLEDGMENTS

The authors are grateful to Professor M. Furukawa for valuable comments and discussions. This work was supported by Grant-in-Aid for Scientific Research (Grant Nos. 14102033 and 19340170) from MEXT, Japan.

[1]R. C. Davidson, *Physics of Nonneutral Plasmas* (Imperial College Press, London, 2001).
[2]D. H. E. Dubin and T. M. O'Neil, Rev. Mod. Phys. **71**, 87 (1999).

[3]J. R. Danielson and T. S. Pedersen, editors, AIP Conf. Proc. **1114** (2009) (entire proceedings).
[4]C. M. Surko and R. G. Greaves, Phys. Plasmas **11**, 2333 (2004).
[5]V. Tsytovich and C. B. Wharton, Comments Plasma Phys. Controlled Fusion **4**, 91 (1978).
[6]N. Iwamoto, Phys. Rev. A **47**, 604 (1993).
[7]E. P. Liang, S. C. Wilks, and M. Tabak, Phys. Rev. Lett. **81**, 4887 (1998).
[8]W. Oohara and R. Hatakeyama, Phys. Rev. Lett. **91**, 205005 (2003).
[9]E. Asseo, Plasma Phys. Controlled Fusion **45**, 853 (2003).
[10]T. Namba, K. Nishihara, T. Yamazaki, S. Asai, and T. Kobayashi, AIP Conf. Proc. **1037**, 56 (2008).
[11]A. P. Mills, Jr., Nucl. Instrum. Methods Phys. Res. B **192**, 107 (2002).
[12]C. M. Surko, M. Leventhal, and A. Passner, Phys. Rev. Lett. **62**, 901 (1989).
[13]R. G. Greaves and C. M. Surko, Phys. Rev. Lett. **75**, 3846 (1995).
[14]M. Amoretti, C. Amsler, G. Bonomi, A. Bouchta, P. Bowe, C. Carraro, C. L. Cesar, M. Charlton, M. J. T. Collier, M. Doser, V. Filippini, K. S. Fine, A. Fontana, M. C. Fujiwara, R. Funakoshi, P. Genova, J. S. Hangst, R. S. Hayano, M. H. Holzscheiter, L. V. Jørgensen, V. Lagomarsino, R. Landua, D. Lindelöf, E. Lodi Rizzini, M. Macrì, N. Madsen, G. Manuzio, M. Marchesotti, P. Montagna, H. Pruys, C. Regenfus, P. Riedler, J. Rochet, A. Rotondi, G. Rouleau, G. Testera, A. Variola, T. L. Watson, and D. P. van der Werf, Nature (London) **419**, 456 (2002).
[15]G. Gabrielse, N. S. Bowden, P. Oxley, A. Speck, C. H. Storry, J. N. Tan, M. Wessels, D. Grzonka, W. Oelert, G. Schepers, T. Sefzick, J. Walz, H. Pittner, T. W. Hänsch, and E. A. Hessels, Phys. Rev. Lett. **89**, 213401 (2002).
[16]N. Kuroda, H. A. Torii, K. Yoshiki Franzen, Z. Wang, S. Yoneda, M. Inoue, M. Hori, B. Juhász, D. Horváth, H. Higaki, A. Mohri, J. Eades, K. Komaki, and Y. Yamazaki, Phys. Rev. Lett. **94**, 023401 (2005).
[17]Z. Yoshida, Y. Ogawa, J. Morikawa, H. Himura, S. Kondoh, C. Nakashima, S. Kakuno, M. Iqbal, F. Volponi, N. Shibayama, and S. Tahara, AIP Conf. Proc. **498**, 397 (1999).
[18]X. Sarasola, T. S. Pedersen, P. W. Brenner, and M. S. Hahn, Contrib. Plasma Phys. **50**, 673 (2010).
[19]C. Nakashima, Z. Yoshida, H. Himura, M. Fukao, J. Morikawa, and H. Saitoh, Phys. Rev. E **65**, 036409 (2002).
[20]H. Saitoh, Z. Yoshida, C. Nakashima, H. Himura, J. Morikawa, and M. Fukao, Phys. Rev. Lett. **92**, 255005 (2004).
[21]H. Saitoh, Z. Yoshida, and S. Watanabe, Phys. Plasmas **12**, 092102 (2005).
[22]J. D. Daugherty, J. E. Eninger, and G. S. Janes, Phys. Fluids **12**, 2677 (1969).
[23]P. Zaveri, P. I. John, K. Avinash, and P. K. Kaw, Phys. Rev. Lett. **68**, 3295 (1992).
[24]J. P. Marler and M. R. Stoneking, Phys. Rev. Lett. **100**, 155001 (2008).
[25]S. Pahari, H. S. Ramachandran, and P. I. John, Phys. Plasmas **13**, 092111 (2006).
[26]H. Himura, H. Wakabayashi, Y. Yamamoto, M. Isobe, S. Okamura, K. Matsuoka, A. Sanpei, and S. Masamune, Phys. Plasmas **14**, 022507 (2007).
[27]J. P. Kremer, T. S. Pedersen, R. G. Lefrancois, and Q. Marksteiner, Phys. Rev. Lett. **97**, 095003 (2006).
[28]Z. Yoshida, Y. Ogawa, J. Morikawa, S. Watanabe, Y. Yano, S. Mizumaki, T. Tosaka, Y. Ohtani, A. Hayakawa, and M. Shibui, Plasma Fusion Res. **1**, 008 (2006).
[29]Y. Ogawa, Z. Yoshida, J. Morikawa, H. Saitoh, S. Watanabe, Y. Yano, S. Mizumaki, and T. Tosaka, Plasma Fusion Res. **4**, 020 (2009).
[30]Z. Yoshida, H. Saitoh, J. Morikawa, S. Watanabe, Y. Yano, S. Mizumaki, T. Tosaka, Y. Ohtani, A. Hayakawa, and M. Shibui, Phys. Rev. Lett. **104**, 235004 (2010).
[31]H. Saitoh, Y. Yano, T. Mizushima, J. Morikawa, and Z. Yoshida, Plasma Fusion Res. **4**, 054 (2009).
[32]J. P. Kremer, T. Sunn Pedersen, Q. Marksteiner, R. G. Lefrancois, and M. Hahn, Rev. Sci. Instrum. **78**, 013503 (2007).
[33]N. Hershkowitz, in *Plasma Diagnostic* (Academic, New York, 1989).
[34]J. W. Berkery, Q. R. Marksteiner, T. S. Pedersen, and J. P. Kremer, Phys. Plasmas **14**, 084505 (2007).
[35]M. Schulz and L. J. Lanzerotti, *Particle Diffusion in the Radiation Belts* (Springer, New York, 1974).
[36]H. Hasegawa, M. Fujimoto, T.-D. Phan, H. Rème, A. Balogh, M. W. Dunlop, C. Hashimoto, and R. TanDokoro, Nature (London) **430**, 755 (2004).
[37]Y. Chen, G. D. Reeves, and R. H. W. Friedel, Nat. Phys. **3**, 614 (2007).
[38]A. Hasegawa, Phys. Scr. **2005**, 72 (2005).
[39]R. H. Levy, J. D. Daugherty, and O. Buneman, Phys. Fluids **12**, 2616 (1969).
[40]A. J. Peurrung, J. Notte, and J. Fajans, Phys. Rev. Lett. **70**, 295 (1993).